IOP Publishing — Journal of Physics D: Applied Physics
J. Phys. D: Appl. Phys. **42** (2009) 234003 (8pp) doi:10.1088/0022-3727/42/23/234003

Parameter extraction of HgCdTe infrared photodiodes exhibiting Auger suppression

P Y Emelie[1], J D Phillips[1], S Velicu[2] and P S Wijewarnasuriya[3]

[1] Department of Electrical Engineering and Computer Science, University of Michigan, Ann Arbor, MI 48109-2122, USA
[2] EPIR Technologies, 590 Territorial Drive, Bolingbrook, IL 60440, USA
[3] US Army Research Laboratory, 2800 Powder Mill Road, Adelphi, MD 20783-1197, USA

E-mail: pyemelie@umich.edu

Received 1 September 2009
Published 17 November 2009
Online at stacks.iop.org/JPhysD/42/234003

Abstract
In this work, finite element methods are used to obtain self-consistent, steady-state solutions of Poisson's equation and the carrier continuity equations. Experimental dark current–voltage characteristics between 120 and 300 K of HgCdTe Auger-suppressed photodiodes with cutoff wavelength of $\lambda_c = 10\,\mu$m at 120 K are fitted using numerical simulations. Fitting parameters used include the overlap integral $|F_1 F_2|$ found to vary from 0.29 at 120 K down to 0.20 at 300 K and the Shockley–Read–Hall (SRH) characteristic lifetime found to be of the order of 10^{-7} s at all temperatures. Based on this fitting, negative differential resistance observed in the experimental data is attributed to full suppression of Auger-1 processes and partial suppression of Auger-7 processes. Leakage current induced by traps and impurities in the material causing SRH recombination is found to limit the saturation current after Auger suppression.

1. Introduction

A nearly universal goal for infrared photon detection systems is to increase their operating temperature without sacrificing performance. The limiting factor for cooling requirements is the dark current in the detector devices. For long-wave infrared (LWIR) HgCdTe infrared photodiodes, Auger generation typically dominates the dark current at elevated temperatures, where the low doped absorber layer becomes intrinsic and the carrier concentration is higher than the doping level. Standard p–n junction photodiodes therefore become very noisy when operated near room temperature. Device designs have been proposed [1] to suppress Auger processes in HgCdTe by reducing carrier densities below thermal equilibrium through the application of a reverse bias.

Auger-suppressed photodiodes consist of a middle lightly doped ν (n-type) or π (p-type) active region which acts as an absorber contacted by heavily doped n+ and p+ larger band gap regions. Auger suppression translates into a negative differential resistance (NDR) in the reverse-bias current–voltage (I–V) characteristics, which has been experimentally observed in devices grown by metal-organic chemical vapour deposition (MOCVD) [2] and molecular beam epitaxy (MBE) using silver as an acceptor dopant [3]. More recently, Wijewarnasuriya *et al* (2008) [4] reported Auger suppression in LWIR MBE-grown devices using arsenic as an acceptor dopant. The carrier concentration profiles and the resulting recombination rates in these devices are highly non-uniform and space-dependent, where previous analytical models [5] of these devices offer only a limited insight. Standard analytical models for HgCdTe infrared photodiodes are also not suited for these devices due to the unique NDR characteristics under reverse bias corresponding to the suppression of Auger processes. We have previously reported a numerical device model to describe the operation of these devices [6–8] with details summarized in appendix A. In this work, we use our numerical device model to fit and analyse the experimental reverse bias current–voltage characteristics of LWIR Auger-supressed photodiodes reported by Wijewarnasuriya *et al* (2008) [4].

2. Experimental

Details of the experimental device fabrication have been reported elsewhere [4]. Here we summarize the information on the devices relevant to our simulation analysis. The final planar device structure is shown in figure 1(*a*). The three-layer P+/π/N+ planar structure was grown by MBE by EPIR Technologies on a lattice-matched CdZnTe substrate. The

 © 2009 IOP Publishing Ltd Printed in the UK

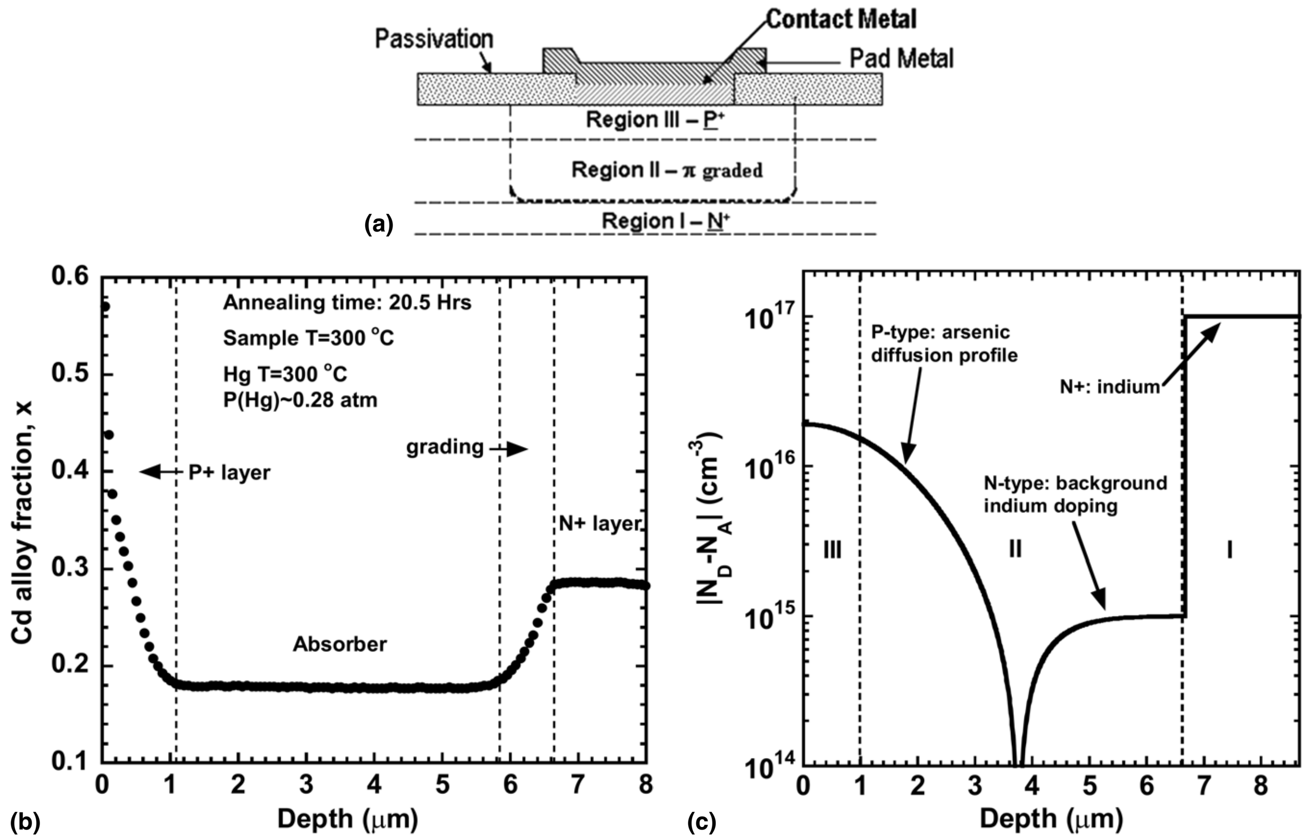

Figure 1. (*a*) Planar device structure, (*b*) Cd alloy composition after annealing obtained by SIMS and (*c*) doping profile in the HOT structure.

bottom $Hg_{1-x}Cd_xTe$ layer, region I, is $\sim 2\,\mu$m thick with designed cadmium fraction $x = 0.30$. The absorber layer, region II, is $\sim 5\,\mu$m thick with designed $x = 0.22$. The measured cutoff wavelength λ_c is $\sim 10.4\,\mu$m at 100 K and $\sim 7.4\,\mu$m at 250 K. The top layer, region III, is $\sim 1\,\mu$m thick with designed $x = 0.30$. The device is designed with a wider band gap ($x = 0.30$) at the top and bottom layers compared with the absorber layer ($x = 0.22$) in order to achieve the exclusion and extraction layers, respectively. The designed Cd alloy composition based on spectroscopic ellipsometry (SE) experimental data measured *in situ* during MBE growth is not the actual value of the device due to interdiffusion during annealing steps, as indicated in the experimental secondary ion mass spectroscopy (SIMS) data shown in figure 1(*b*). These data show the Cd alloy composition measured after the deep diffusion annealing step under low Hg partial pressure P(Hg) to obtain p-type doping in the absorber layer. We observe that the top P+ layer is converted continuously to a higher x composition because not enough Hg is being provided to compensate for Hg out-diffusion. This has also been observed previously [9]. Region I is *in situ* heavily doped n-type with indium concentration of $10^{17}\,\mathrm{cm}^{-3}$. The background concentration in regions II and III is n-type with indium at $\sim 10^{15}\,\mathrm{cm}^{-3}$. The *ex situ* p-type doping of the absorber and the top layers was achieved using arsenic implantation, followed by a deep diffusion anneal under low P(Hg) as described previously [4]. Typical SIMS profiles show an arsenic concentration in the low $10^{16}\,\mathrm{cm}^{-3}$ for the top layer and an arsenic concentration in the range 10^{15}–$10^{16}\,\mathrm{cm}^{-3}$ for the absorber layer. Figure 1(*c*) shows the doping profile in the device. A Gaussian curve is used to represent the p-type arsenic implant/diffusion experimental SIMS profile. The n-type doping profile in the device is taken from designated values for *in situ* indium doping of HgCdTe during MBE growth. The surface is then passivated by deposition of ZnS, and the p-type and n-type metal contacts are formed by gold evaporation.

Planar circular devices with varying diameters were fabricated. Figure 2 shows the current–voltage characteristics at 300 K for selected HgCdTe P+/π/N+ devices. The photodiode reverse-bias leakage current seems to be limited by a *series resistance* in the device up to $\sim$400 mV. It also shows a *strong* NDR at $\sim$400–500 mV which we attribute to *strong Auger suppression* in the device. We observe $\sim$50% decrease in the dark current at room temperature which is consistent with previous results obtained on HgCdTe P+/ν/N+ mesa devices grown by MOCVD [2] and MBE [3]. Traces from similar devices coincide very well, indicating a good uniformity of the layer. The residual differences are attributable to non-uniformities in the processing. The onset voltage of Auger suppression appears to occur at different voltages for the two different device diameters. This is due to the different voltage drop across the series resistances for the two sets of diodes.

Figure 3 shows the temperature-dependent current–voltage characteristics for one selected device. NDR is observed between 120 and 300 K, becoming higher as the temperature is increased, which is consistent with clear Auger suppression in the device. The onset voltage of Auger

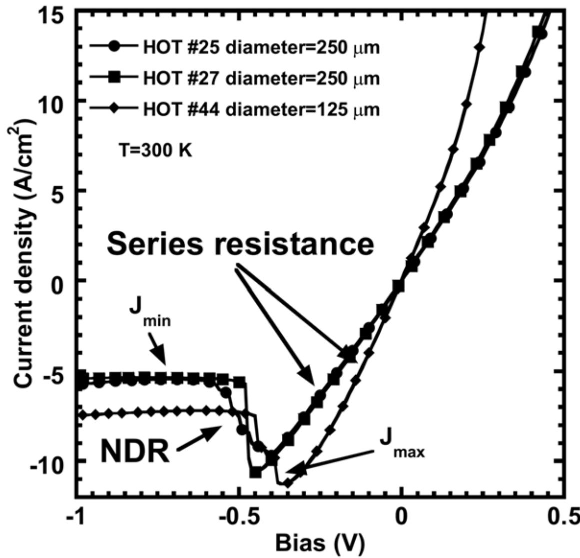

Figure 2. Current–voltage characteristics at 300 K for selected devices.

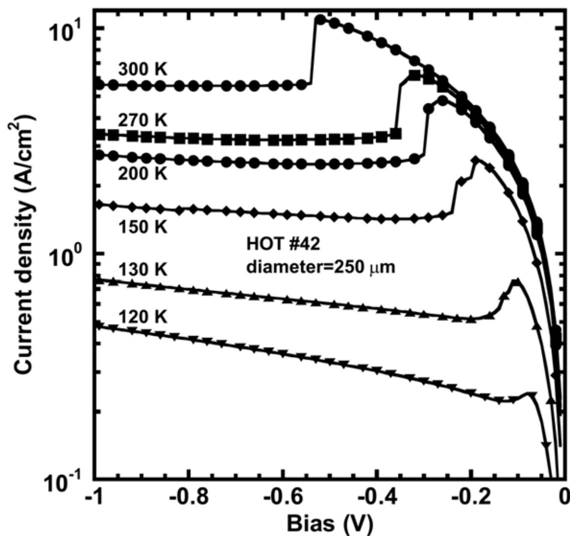

Figure 3. Reverse-bias current–voltage characteristics for HOT #42 at different temperatures.

suppression decreases as the temperature is decreased. This onset voltage at a particular temperature is the result of the series resistance in the device, which increases as the temperature is decreased, and the photodiode leakage current magnitude, which decreases as the temperature is decreased. After Auger suppression, the dark current saturates up to a certain bias voltage. The dark current increases above this voltage, a behaviour that may be attributed to tunnelling processes in the LWIR HgCdTe photodiode based on the observation of a decreasing onset voltage for tunnelling with decreasing temperature.

3. Device simulation

3.1. Simulation methodology

Steady-state numerical simulations are performed using Sentaurus device [10], a commercial package by Synopsys. Sentaurus device self-consistently determines a full coupled solution of Poisson's equation and the continuity equations for electrons and holes using an approximate Newton method [11] with Gaussian elimination. Fermi–Dirac statistics is used. HgCdTe material and recombination parameters—considering Auger, radiative and Shockley–Read–Hall (SRH) recombination—are included in the model. Carrier degeneracy and conduction band non-parabolicity are also taken into account. Surface recombination and tunnelling mechanisms are not accounted for in the simulations. Simulation output calculations of electrical and optical characteristics of HgCdTe p–n infrared photodiodes are comparable to published experimental data from different sources for both mid-wave infrared (MWIR) and LWIR [8]. The Cd alloy profile, including compositional grading at the two junctions, is taken from experimentally measured SE data and included in the simulation using a linear interpolation of the HgCdTe material parameters.

The calculated energy band diagram for this device at 1 V reverse bias and $T = 300$ K is shown in figure 4(*a*). *Partial depletion of the absorber layer* is achieved by increasing the reverse bias (depletion width is ~2–2.5 μm). The calculated equilibrium and non-equilibrium (1 V reverse bias) carrier concentration is shown in figure 4(*b*). Under equilibrium, the LWIR absorber layer is essentially intrinsic. As the reverse bias is increased, the electron and hole concentration decreases by several orders of magnitude due to the effect of the exclusion/extraction layers. The hole concentration decreases down to the extrinsic p-type doping level for a depth $<4\,\mu$m (non-depleted region). This initial simulation confirms that the NDR observed experimentally is likely due to strong Auger suppression in the device, but further analysis is required. More can be learned by fitting the experimental device data using our device model.

3.2. Fitting methodology

Our device model is used to fit the temperature-dependent current–voltage data of HOT #42 shown in figure 3. We perform a 1D simulation of a cross-section of the device. In order to fit the I–V data for each temperature (120, 130, 150, 200, 270, 300 K), we fit the maximum leakage current experimental value before Auger suppression (J_{max}) and the minimum leakage current experimental value after Auger suppression (J_{min}) as illustrated in figure 2. In our model, J_{min} is taken as the calculated current density at 500 mV reverse bias which is found to be high enough for dark current saturation (neglecting the series resistance). J_{max} is taken as the maximum calculated current density between zero bias and 500 mV reverse bias. The temperature-dependent experimental values for J_{min} and J_{max} that we are fitting are shown in figure 5, along with the corresponding experimental reverse-bias value.

Based on figure 1(*b*), we set the Cd alloy composition profile in the top P+ layer, x(III), as a fitting parameter in the form of a linear grading $x_{top} \rightarrow 0.3$ (with $x_{top} > 0.3$). The other two fitting parameters are the ones that are found to have the most influence on the calculated device

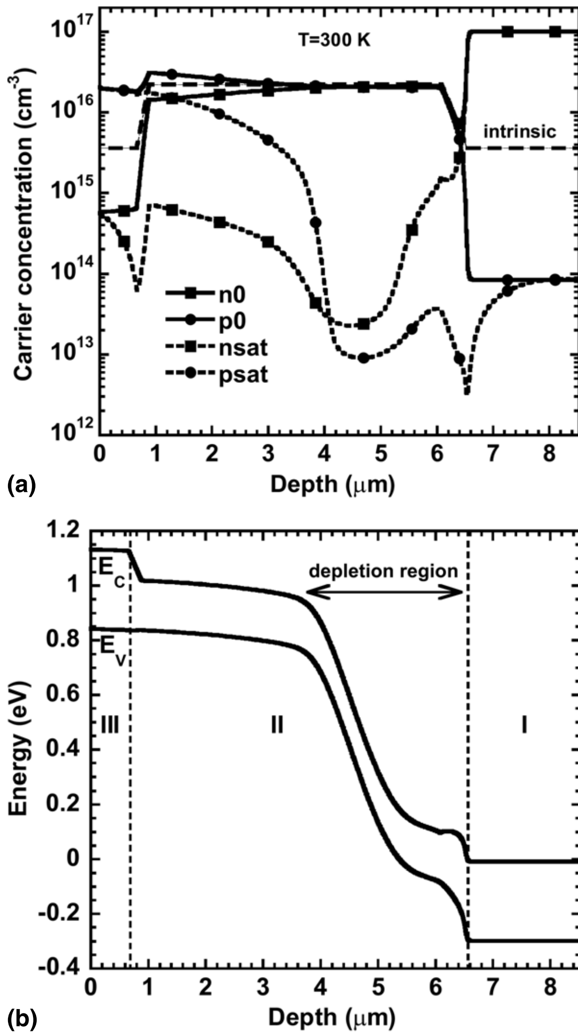

Figure 4. (*a*) Calculated energy band diagram of the HOT structure at $T = 300$ K and 1 V reverse bias and (*b*) electron and hole carrier concentration in the structure at zero bias and 1 V reverse bias. Also shown is the intrinsic carrier level (dashed line).

characteristics: $|F_1F_2|$ in the absorber layer which is related to the magnitude of Auger-1 processes (appendix A), and the SRH characteristic lifetime $\tau_{n0} = \tau_{p0}$ (assuming the same for electrons and holes) in the absorber layer which is related to the concentration of traps, impurities, dislocations or other elements causing SRH recombination as well as their capture cross-sections (appendix A). At this time, there is no clear agreement on the value of $\gamma = \tau^{i}_{A7}/\tau^{i}_{A1}$ in HgCdTe which is related to the magnitude of Auger-7 processes. Consequently, we set $\gamma = 6$ in this study which is the most common value used. Figure 6 shows the effect of each of these two parameters (for a given x(III)) on the calculated I–V at 300 K. We observe that $|F_1F_2|$ mostly has an influence on the value of $(J_{max} - J_{min})$ and therefore the strength of the NDR. The SRH lifetime τ_{n0} (τ_{p0}) has an influence on the values of both J_{min} and J_{max}, but mostly on J_{min}. Table 1 summarizes the parameters used in our device model to fit the experimental I–V characteristics. In this case, the temperature dependence of $|F_1F_2|$ and τ_{n0} (τ_{p0}) is taken into account. The Cd alloy profile in the top P+ layer x(III) is constant with temperature. The doping profile in

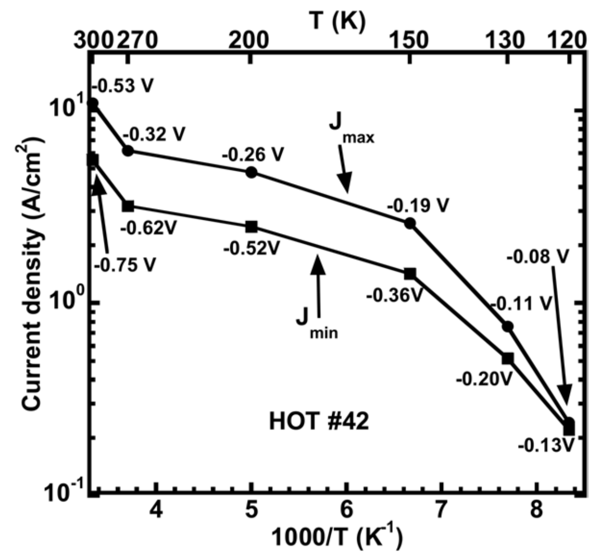

Figure 5. Experimental absolute value of the current densities J_{min} and J_{max} versus temperature from HOT #42.

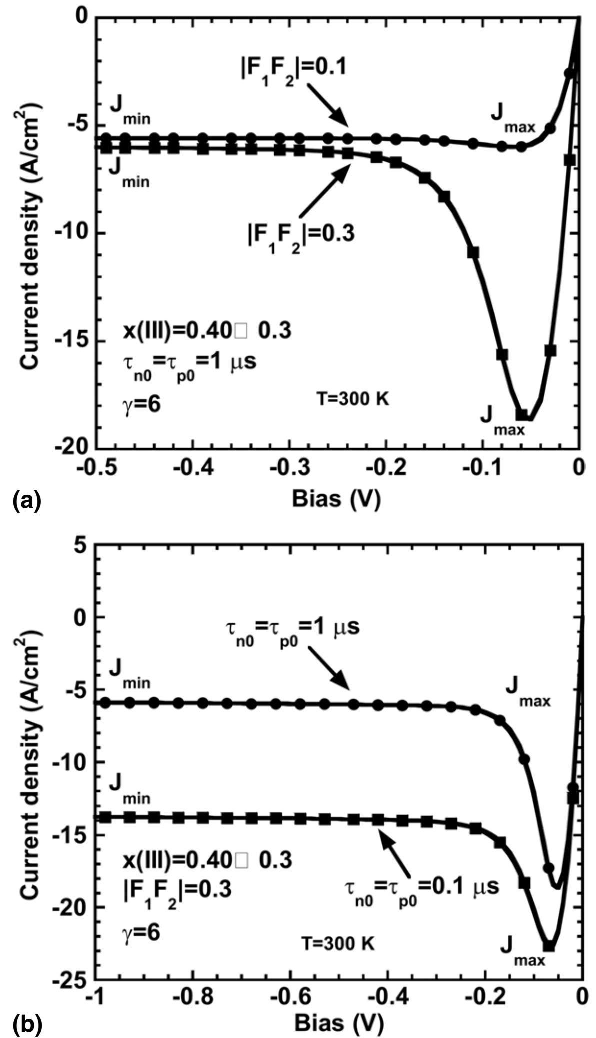

Figure 6. Calculated I–V at 300 K for two different values of (*a*) $|F_1F_2|$ and (*b*) τ_{SRH}.

Table 1. Material parameters used for I–V fitting.

	Bottom N+ layer (Region I)	Absorber π layer (Region II)	Top P+ layer (Region III)
Thickness	2 μm	5.2 μm	0.66 μm
Cd fraction x	0.3	0.22	Fitting parameter: Grading $x_{top} \rightarrow 0.3$
Overlap integral $\|F_1F_2\|$	0.3	Fitting parameter	0.3
γ-ratio	6	6	6
SRH trap level E_{trap}	Intrinsic Fermi E_{Fi}	Intrinsic Fermi E_{Fi}	Intrinsic Fermi E_{Fi}
$\tau_{n0} = \tau_{p0}$	1 μs	Fitting parameter	1 μs

Table 2. Fitting parameters. $R^2 > 0.99$ for the fittings of both J_{max} and J_{min}.

					J_{max} (A cm^{-2})		J_{min} (A cm^{-2})	
T (K)	x(III)	$\|F_1F_2\|$	$\tau_{n0} = \tau_{p0}$ (s)	R_{series} (Ω)	Exp.	Sim.	Exp.	Sim.
120	Linear grading:	0.29	2.8×10^{-7}	334	0.24	0.24	0.22	0.21
130	0.41 → 0.3	0.28	3.3×10^{-7}	216	0.76	0.75	0.52	0.51
150		0.26	3.7×10^{-7}	125	2.60	2.51	1.42	1.49
200		0.25	3.8×10^{-7}	98	4.78	4.85	2.49	2.41
270		0.21	3.5×10^{-7}	92	6.19	6.12	3.19	3.21
300		0.20	3.4×10^{-7}	89	10.96	10.83	5.54	5.52

figure 1(c) and device geometry are taken from experimental data and designated values. Compositional grading between each region interface is taken into account. An iteration scheme described in detail elsewhere [8] is used to obtain the best values for each fitting parameter. The fitting for each temperature is obtained after 2–3 iterations maximum.

Ultimately, the goal of this fitting is to understand what mechanisms are limiting the leakage current just before (J_{max}) and after (J_{min}) Auger suppression. The total leakage current J_{tot} can be expressed as the sum of the electron diffusion current in the top P+ layer, $J_{n,diff}$ (P+), the hole diffusion current in the bottom N+ layer, $J_{p,diff}$ (N+), and the absorber layer current J_{abs}:

$$J_{tot} = J_{n,diff}(P+) + J_{abs} + J_{p,diff}(N+). \qquad (1)$$

As seen in figure 4(a), the absorber layer current is a combination of diffusion and g-r current, depending on the reverse bias. However, it is much more interesting to define it as the sum of an Auger-1 current in the absorber, J_{A1}, an Auger-7 current in the absorber, J_{A7}, and a SRH current in the absorber, J_{SRH}:

$$J_{abs} = J_{A1} + J_{A7} + J_{SRH}. \qquad (2)$$

This way, we can determine the recombination mechanisms limiting the leakage current in the HgCdTe HOT photodiodes. J_{min} and J_{max} are fitted at each temperature using the set of three fitting parameters described earlier, and we extract from our simulation calculations the corresponding value for each current component mentioned in these last two equations. The values for the Auger and SRH currents in the absorber are determined by switching 'on' and 'off' each recombination mechanism separately in our device model. The fitting result is presented in the following section.

3.3. Fitting results

The fitting procedure results in a Cd alloy profile in the top P+ layer x(III) = 0.300–0.414. Table 2 summarizes the fitting parameters for each temperature. Both the assumption made about x(III) and its fitting value are consistent with experimental SIMS data shown in figure 1(b). The parameter x(III) is mainly a factor for $T > 270$ K. As a result, the primary two fitting parameters are $|F_1F_2|$ and τ_{SRH}. Given the assumptions made in this fitting, the presence of only two primary fitting parameters, and fitting for a range of temperatures, we are confident that a unique solution is obtained. R^2 values for the fitting of J_{max} and J_{min} support this assertion as they are both greater than 0.99. In addition, the different values found for $|F_1F_2|$ in the device absorber are within the range of reported values for Auger in HgCdTe (0.1–0.3). There is no clear agreement on the temperature dependence of $|F_1F_2|$, where the extracted values of $|F_1F_2| \sim 0.3$ at 120 K decreasing to $|F_1F_2| \sim 0.2$ at 300 K require further investigation. The fitting parameter τ_{n0} (τ_{p0}) is related to the inverse product of trap concentration, capture cross-section and thermal velocity v_{th}. The trap concentration and capture cross-section can be considered constant with temperature. Therefore, τ_{n0} (τ_{p0}) is expected to vary as $1/v_{th}$ with temperature. Figure 7 shows that the fitting parameter τ_{n0} (τ_{p0}) indeed varies as $1/v_{th}$ for $T > 150$ K. For $T < 150$ K, τ_{n0} (τ_{p0}) deviates from the $1/v_{th}$ trend, which may be attributed to tunnelling processes in the devices such as trap-assisted tunnelling (TAT). Tunnelling processes are expected to appear at low temperatures in LWIR HgCdTe devices. Fitting the full I–V was used to validate this study and is shown elsewhere [8].

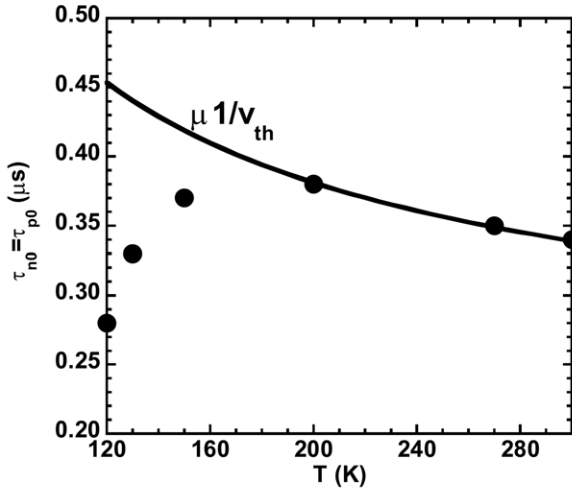

Figure 7. Fitting parameter τ_{n0} (τ_{p0}) versus temperature and guide to dependence on v_{th}.

3.4. Discussion of J_{max} and J_{min}

Figure 8(*a*) shows the calculated magnitude of J_{max} after fitting, along with the different magnitudes of the leakage current components. According to our fitting result, the maximum current *before Auger suppression*, J_{max}, is limited by a SRH current in the absorber at $T = 120$ K. This SRH current obtained in our model may be associated in the experimental device with a background trap concentration introduced during growth and/or processing. This SRH current has a weak dependence on temperature. It can also be related to threading dislocations in the device as we have described previously causing SRH recombination and/or TAT, especially at lower temperatures as confirmed by a decreasing fitted τ_{n0} (τ_{p0}) as the temperature is decreased. Determining the real causes and origins of this SRH current would require more information about the devices than we currently have. Therefore, we will leave this analysis for future work. We simply point out that, according to our model, the level of SRH is relatively high in these devices in the whole temperature range and that SRH recombination is the limiting mechanism for J_{max} up to ~130–140 K. At $T = 120$ K, both Auger-1 and Auger-7 currents in the absorber are very low compared with J_{SRH} because the intrinsic carrier concentration in the absorber is still relatively low. However, both currents rapidly increase as the temperature is increased. The Auger-1 current in the absorber limits J_{max} above ~130–140 K. Finally, the hole diffusion current in the bottom N+ layer stays relatively weak at all temperatures. The electron diffusion current in the top P+ layer has some influence on J_{max} above 270 K.

Figure 8(*b*) shows the calculated magnitude of J_{min} after fitting, along with the different magnitudes of the leakage current components. According to our fitting result, the maximum current *after Auger suppression* (and before tunnelling processes), J_{min}, is limited by a SRH current in the absorber between 120 K and room temperature. This confirms what we observed in the analysis of J_{max}, which is that there is a high concentration of traps/dislocations. This is expected in LWIR HgCdTe and can be reduced as the HgCdTe growth

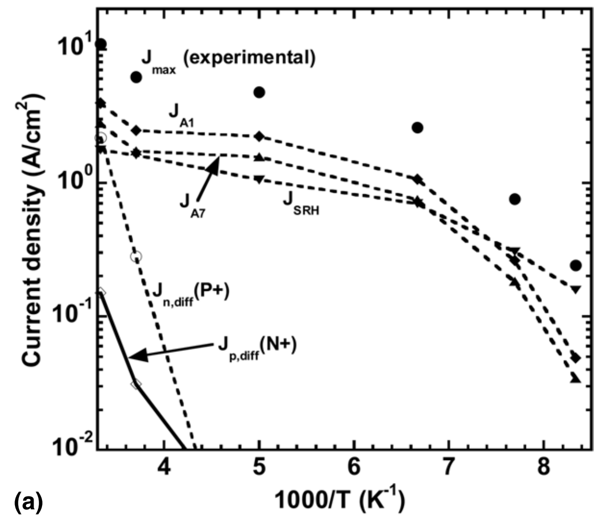

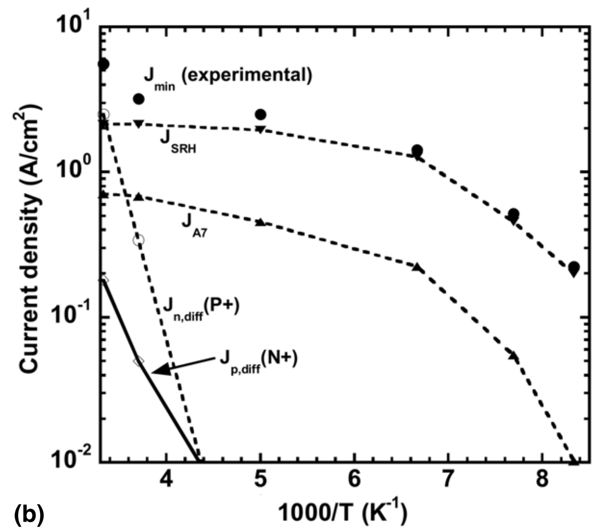

Figure 8. (*a*) Experimental values for J_{max} versus temperature. Also shown are the calculated Auger-1 current in the absorber J_{A1}, Auger-7 current in the absorber J_{A7}, SRH current in the absorber J_{SRH}, electron diffusion current in the top P+ layer $J_{n,diff}$(P+) and hole diffusion current in the bottom N+ layer $J_{p,diff}$(N+). (*b*) Experimental values for J_{min} versus temperature. Also shown are the Auger-7 current in the absorber J_{A7}, SRH current in the absorber J_{SRH}, electron diffusion current in the top P+ layer $J_{n,diff}$(P+) and hole diffusion current in the bottom N+ layer $J_{p,diff}$ (N+).

and processing technology develops. The Auger-1 current J_{A1}, which was found to limit J_{max} in figure 8(*a*), *is fully suppressed* as the reverse bias is increased and is therefore not shown in figure 8(*b*). The Auger-7 current in the absorber J_{A7} increases as the temperature is increased. Although it is not found to limit J_{min}, it shows that the Auger-7 current is only partially suppressed in the device. The 'residual' Auger-7 current arises from the extrinsic p-type doping level in the absorber which ranges from 10^{15} to 10^{16} cm^{-3} as seen in figure 8(*a*). The amount of Auger-7 suppression is ~70% according to our results. The hole diffusion current in the bottom N+ layer stays relatively weak at all temperatures, as observed when analysing J_{max}. The electron diffusion current in the top P+ layer has some influence on J_{min} above 270 K. This analysis gives us significant insight on the limiting leakage current mechanisms

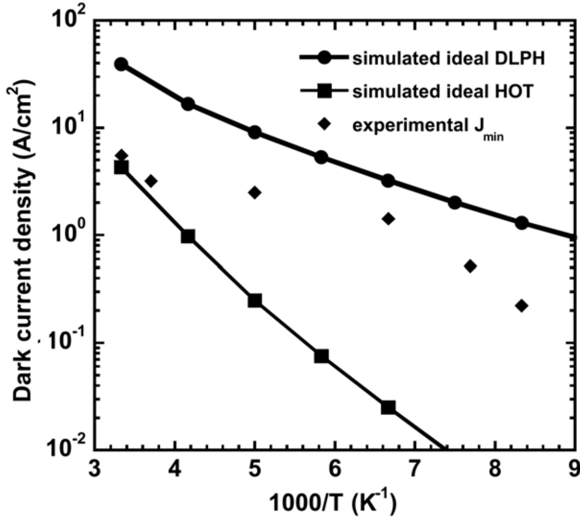

Figure 9. Calculated dark current density at 200 mV reverse bias for an ideal DLPH and HOT devices (with $x(\mathrm{abs}) = 0.22$) and experimental J_{min} versus temperature.

in experimental LWIR HOT devices, both *before* and *after* Auger suppression.

3.5. Performance improvement

Finally, the saturation current in our experimental device (J_{min}) is compared with the one in a standard HgCdTe DLPH photodiode simulated using our device model. We also compare J_{min} with the dark current in a simulated ideal HOT photodiode with the same fixed cutoff wavelength as the experimental device ($\sim$10.4 μm at 100 K). We plot the dark current at 200 mV reverse bias versus T using our numerical model for ideal HOT and DLPH photodiodes ($x(\mathrm{abs}) = 0.22$), characterized by a low n-type doping in the absorber, $N_{\mathrm{D}}(\mathrm{absorber}) = 1 \times 10^{15}\,\mathrm{cm}^{-3}$, and a much longer $\tau_{\mathrm{n0}} = \tau_{\mathrm{n0}} = 5\,\mu$s than what we observed experimentally. As seen in figure 9, the fabricated HOT device gives a lower saturation current J_{min} than for the ideal DLPH at all temperatures. Above $\sim$200 K, both ideal and experimental HOT devices have comparable dark current. Below 200 K, the experimental HOT device has a much larger saturation current than the ideal HOT device which shows the room for improvement that can be achieved by optimizing the growth and fabrication process. Improvements are especially needed in terms of lower doping levels in the absorber layer and less traps/dislocations causing SRH recombination.

4. Conclusions

The experimental HgCdTe Auger-suppressed infrared devices were simulated using our numerical model. By fitting the temperature-dependent current–voltage experimental data for one selected device where clear NDR is observed, we confirmed that the NDR is due to Auger suppression. More specifically, NDR is attributed to full suppression of Auger-1 processes and partial suppression of Auger-7 processes. The percentage of Auger-7 suppression is $\sim$70%. After Auger suppression, the remaining leakage current is mostly limited by a high SRH recombination component in these devices. This component can be due to a high concentration of traps and dislocations in these HgCdTe HOT layers, especially the LWIR absorber which is more sensitive to the growth and processing. Part of the leakage current is also due to a 'residual' Auger-7 current in the absorber due to the extrinsic p-type doping level which ranges from 10^{15} to $10^{16}\,\mathrm{cm}^{-3}$.

Appendix A: Simulation model

The partial differential equations are discretized in the simulation grid using a finite-difference discretization based on the box method [12] and the Scharfetter–Gummel method and solved at each node. In the case of current–voltage calculations, this method is typically estimated to give a maximum error of $\pm$10%. In the case of ohmic contacts, simple Dirichlet boundary conditions are applied, where the surface potential ψ_{s} and electron and hole concentrations, n_{S} and p_{S}, are fixed. The electron and hole quasi-Fermi potentials are equal and are set to the applied bias of that electrode, i.e. $E_{\mathrm{Fn}} = E_{\mathrm{Fp}} = V_{\mathrm{applied}}$. The surface potential ψ_{s} is fixed at a value consistent with the charge neutrality condition:

$$n_{\mathrm{S}} - p_{\mathrm{S}} = N_{\mathrm{D}} - N_{\mathrm{A}}. \tag{A.1}$$

Auger, radiative and SRH recombination are included at any location within the device. We consider Auger-1 using Blakemore [13] for the intrinsic Auger-1 lifetime $\tau_{\mathrm{A1}}^{\mathrm{i}}$ (A.3) and Auger-7 using Casselman and Petersen [14] for the intrinsic Auger-7 lifetime $\tau_{\mathrm{A7}}^{\mathrm{i}}$ (A.4). The following expression for the Auger recombination rate ($\mathrm{cm}^{-3}\,\mathrm{s}^{-1}$) is based on Beattie and Landsberg [15]:

$$U_{\mathrm{Auger}}^{\mathrm{net}} = G_{\mathrm{A1}}\left(pn^2 - nn_{\mathrm{i}}^2\right) + G_{\mathrm{A7}}\left(np^2 - pn_{\mathrm{i}}^2\right), \tag{A.2}$$

$$G_{\mathrm{A1}} = \frac{1}{n_{\mathrm{i}}^2\tau_{\mathrm{A1}}^{\mathrm{i}}} = \left[2n_{\mathrm{i}}^2\frac{3.8\times10^{-18}\varepsilon_{\mathrm{s}}^2\left(1+\frac{m_{\mathrm{e}}^*}{m_{\mathrm{h}}^*}\right)^{0.5}\left(1+2\frac{m_{\mathrm{e}}^*}{m_{\mathrm{h}}^*}\right)}{m_{\mathrm{e}}^*\left|F_1F_2\right|^2\left(\frac{kT}{E_{\mathrm{G}}}\right)^{1.5}}\right.$$
$$\left.\times\exp\left(\frac{1+2\frac{m_{\mathrm{e}}^*}{m_{\mathrm{h}}^*}}{1+\frac{m_{\mathrm{e}}^*}{m_{\mathrm{h}}^*}}\frac{E_{\mathrm{G}}}{kT}\right)\right]^{-1}, \tag{A.3}$$

$$G_{\mathrm{A7}} = \frac{1}{n_{\mathrm{i}}^2\tau_{\mathrm{A7}}^{\mathrm{i}}} = G_{\mathrm{A1}}\left[\frac{\gamma'\left(1-\frac{5E_{\mathrm{G}}}{4kT}\right)}{1-\frac{3E_{\mathrm{G}}}{2kT}}\right]^{-1}, \tag{A.4}$$

$$\frac{\tau_{\mathrm{A7}}^{\mathrm{i}}}{\tau_{\mathrm{A1}}^{\mathrm{i}}} = \frac{\gamma'\left(1-\frac{5E_{\mathrm{G}}}{4kT}\right)}{1-\frac{3E_{\mathrm{G}}}{2kT}} = \gamma, \tag{A.5}$$

where n_{i} is the intrinsic carrier concentration (cm^{-3}), m_{e}^* and m_{h}^* are the electron and hole effective mass, respectively (m_0), and E_{G} is the band gap (eV). The overlap integral $|F_1F_2|$ is taken as fitting parameter in our study. The expression used for the radiative recombination rate ($\mathrm{cm}^{-3}\,\mathrm{s}^{-1}$) is shown here:

$$U_{\mathrm{rad}}^{\mathrm{net}} = G_{\mathrm{R}}\left(np - n_{\mathrm{i}}^2\right), \tag{A.6}$$

$$G_{\mathrm{R}} = 5.8\times10^{-13}\varepsilon_{\mathrm{S}}^2\left(\frac{m_0}{m_{\mathrm{e}}^*+m_{\mathrm{h}}^*}\right)^{1.5}\left(1+\frac{m_0}{m_{\mathrm{e}}^*}\right)\left(\frac{300}{T}\right)^{1.5}$$
$$\times\left(E_{\mathrm{g}}^2 + 3ktE_{\mathrm{g}} + 3.75k^2T^2\right). \tag{A.7}$$

The following expression is used for the SRH recombination rate (cm^{-3} s^{-1}):

$$U_{SRH}^{net} = \frac{np - n_i^2}{\tau_{p0}(n + n_1) + \tau_{n0}(p + p_1)}, \quad (A.8)$$

$$n_1 = n_i e^{\frac{E_{trap}}{kT}}, \quad (A.9)$$

$$p_1 = n_i e^{-\frac{E_{trap}}{kT}}, \quad (A.10)$$

where the defect level E_{trap} is taken to be at the intrinsic Fermi level, we assume neutral SRH centres, and τ_{n0} and τ_{p0} are referred to as electron and hole characteristic SRH lifetimes and are used as fitting parameters in our study. $Hg_{1-x}Cd_xTe$ material parameters including band gap energy, electron affinity, dielectric constant and carrier mobility are taken from published data [16]. In particular, the band gap was obtained from Hansen *et al* [17], the low-field electron mobility was taken from the empirical formula based on Scott's Hall data [18] and the hole mobility is assigned as 1% of the electron mobility. The electron effective mass is taken from Weiler's expression [19] using $E_p = 19$ eV, the spin–orbit splitting energy $\Delta = 1$ eV and $F = -0.8$. The hole effective mass is fixed at 0.55 m_0 which is in the range of heavy-hole effective masses reported previously [20]. The intrinsic carrier concentration is taken from the Hansen and Schmidt [21] empirical formula.

References

[1] Elliott C T and Ashley T 1985 *Electron. Lett.* **21** 451
[2] Maxey C D, Jones C L, Metcalfe N E, Catchpole R A, Gordon N T, White A M and Elliott C T 1997 *Proc. SPIE* **3122** 453
[3] Skauli T, Steen H, Colin T, Hegelsen P, Lovold S, Elliott C T, Gordon N T, Phillips T J and White A M 1996 *Appl. Phys. Lett.* **68** 9
[4] Wijewarnasuriya P S, Emelie P Y, D'Souza A, Brill G, Stapelbroek M G, Velicu S, Chen Y, Grein C H, Sivananthan S and Dhar N K 2008 *J. Electron. Mater.* **37** 1283
[5] Ashley T, Elliott C T and Harker A T 1986 *Infrared Phys.* **26** 303
[6] Emelie P Y, Phillips J D, Velicu S and Grein C H 2007 *J. Electron. Mater.* **36** 846
[7] Emelie P Y, Velicu S, Grein C H, Phillips J D, Wijewarnasuriya P S and Dhar N K 2008 *J. Electron. Mater.* **37** 1362
[8] Emelie P Y 2009 *PhD Thesis* University of Michigan
[9] Bubulac L O, Irvine S J C, Gertner E R, Bajaj J, Lin W P and Zucca R 1993 *Semicond. Sci. Technol.* **8** S270
[10] Synopsis 2005 *Sentaurus Device User Guide* (Mountain View, CA: Synopsys)
[11] Bank R E and Rose D J 1981 *Numer. Math.* **37** 279
[12] Bank R E, Rose D J and Fichtner W 1983 *IEEE T. Electron Dev.* **30** 1031
[13] Blakemore J S 1962 *Semiconductor Statistics* (Oxford: Pergamon)
[14] Casselman T N and Petersen P E 1980 *Solid State Commun.* **33** 615
[15] Beattie A and Landsberg P T 1959 *Proc. R. Soc.* A **249** 16
[16] Wenus J, Rutkowski J and Rogalski A 2001 *IEEE Trans. Electron Dev.* **48** 1326
[17] Hansen G L, Schmidt J L and Casselman T N 1982 *J. Appl. Phys.* **53** 7099
[18] Scott W 1972 *J. Appl. Phys.* **43** 1055
[19] Weiler M 1981 *Semicond. Semimet.* **16** 119
[20] Miles R W 1994 Electron and hole effective masses in HgCdTe *Properties of Narrow Gap Cadmium-based Compounds* ed P Capper (London: INSPEC)
[21] Hansen G L and Schmidt J L 1983 *J. Appl. Phys.* **54** 1639